Proceedings of the
Annual Stability Conference
Structural Stability Research Council
Charlotte, North Carolina, April 11-14, 2023

Flexural behavior of wire arc additively manufactured tubular sections

Cheng Huang[1], Xin Meng[2], Leroy Gardner[3]

Abstract

Wire arc additive manufacturing (WAAM) is a promising metal 3D printing technique in the construction industry for its ability to produce large and complex-shaped elements, with reasonable printing accuracy, time and costs. There is currently, however, a lack of fundamental test data on the structural performance of WAAM elements. To address this, an experimental study into the cross-sectional behavior of WAAM tubular beams has been conducted and is presented herein. A total of 14 stainless steel square, rectangular and irregular hollow sections, spanning over all cross-section classes of EN 1993-1-4 and AISC 370, were tested in four-point bending. 3D laser scanning, silicone casting and Archimedes' measurements were employed to collectively determine the as-built geometry and local geometric imperfections of the test specimens, while digital image correlation (DIC) was used to monitor the deformation responses of the specimens during testing. The full moment-curvature histories and key experimental results are presented and discussed. Similar cross-sectional behavior to that of equivalent, conventionally manufactured sections was observed, with the more slender cross-sections showing increased susceptibility to local buckling. However, owing to the inherent geometric variability of WAAM, the tested 3D printed beams exhibited more variable flexural capacities between the repeat specimens than is generally displayed by conventionally produced stainless steel sections. Finally, the test results were used to assess the applicability of current cross-section design provisions in the European (EN 1993-1-4) and American (AISC 370) structural design specifications, as well as the continuous strength method (CSM), to WAAM stainless steel tubular beams.

1. Introduction

Utilizing incremental layer-by-layer deposition of material to build components, additive manufacturing (AM) has gained considerable industry and academic attention in recent decades, primarily due to its potential for automation and its flexibility in fabricating complex-shaped structures. With advances in technology, AM systems can now be applied to a variety of materials, including polymers, ceramics, concrete and metals, and are being increasingly implemented across multiple industries, such as aerospace, biomedicine and automotive. In

---

[1] Research Associate, Imperial College London, <cheng.huang118@imperial.ac.uk>
[2] Research Associate, Imperial College London, <xin.meng15@imperial.ac.uk>
[3] Professor, Imperial College London, <leroy.gardner@imperial.ac.uk>

particular, the recent emergence of metal additive manufacturing is poised to have a substantial impact on the construction industry (Huang et al. 2022a; Gardner et al. 2023).

The main types of metal AM set out in ISO/ASTM 52900 include sheet lamination, powder bed fusion (PBF) and directed energy deposition (DED); the latter can be further classified into powder-based and wire-based DED according to the form of the feedstock material. Among these metal AM techniques, sheet lamination is unlikely to be able to fabricate the geometric complexity or scale of parts required for construction; PBF and powder-based DED techniques have maximum part size limitations with lengthy build times and high costs, despite the ability to print high complexity and high quality parts. In contrast, wire-based DED techniques provide a higher building speed and significantly expand the maximum part size that can be built, though with compromises on dimensional accuracy and surface quality. Wire arc additively manufacturing (WAAM), a wire-based DED technique that uses metal wire feedstock and a welding arc to build up parts in layers, is deemed to be well suited to structural engineering applications in terms of build scale, speed and cost (Huang et al. 2022b).

Although WAAM has great potential for the construction sector, WAAM is still at the nascent stage and its use in the construction sector has only emerged in recent years. A landmark demonstrator of WAAM for structural use is the MX3D bridge (Gardner et al. 2020), which is a 10.5 m span 3D printed stainless steel footbridge and the first of its kind. This bridge project has launched a comprehensive series of experiments, comprising tensile coupon testing (Kyvelou et al. 2020), cross-section bucking testing (Kyvelou et al. 2021; Huang et al. 2022c), member buckling testing (Huang et al. 2022d) and full-scale structural testing (Gardner et al. 2020), to understand better the performance of WAAM structures.

In this paper, four-point bending tests on 14 WAAM stainless steel beams with square, rectangular and irregular hollow section profiles, printed using the same feedstock material and process parameters as used for the MX3D bridge, are presented. Key mechanical properties determined from previous tensile coupon tests (Kyvelou et al. 2020) on the examined WAAM material are first summarized. The manufacture, geometric measurements and four-point bending tests of the WAAM beams are then described, followed by a discussion of the obtained test results. Lastly, the experimental results are used to assess the existing slenderness limits and the cross-section resistance predictions from EN1993-1-4, AISC 370 and the continuous strength method (CSM).

2. Material tests

To determine the stress-strain response of the WAAM material, tensile tests on coupons extracted from stainless steel plates printed in the same manner as the studied beams were conducted. Coupons extracted from both as-built and machined WAAM plates at 0°, 45° and 90° relative to the deposition direction (see Fig. 1) were tested, to investigate the material anisotropy and the influence of the geometric variability on the resulting mechanical properties. The detailed testing procedure has been described by Kyvelou et al. (2020), while the key test results are summarized in this section. The obtained key material properties for both as-built and machined coupons of two nominal thicknesses t_{nom} are presented in Table 1, including the Young's modulus E, 0.2% and 1.0% proof stresses, $\sigma_{0.2}$ and $\sigma_{1.0}$, ultimate strength σ_{u} and ultimate strain ε_{u}, as well as the strain hardening exponents n, $m_{1.0}$ and m_{u} of the compound Ramberg-

Osgood material model (Ramberg and Osgood 1943; Mirambell and Real 2000; Huang et al. 2023). Note that only the material properties of the θ = 90° coupons (as defined in Fig. 1), which correspond to loading in the longitudinal direction of the beams, are presented herein; the mechanical properties obtained from the material tests are used in Sections 5 and 6 for the analysis of the test results of the studied WAAM beams.

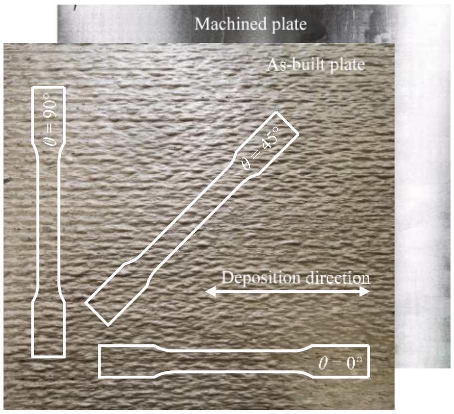

Figure 1: As-built and machined WAAM plates and extraction directions of tensile coupons

Table 1: Average measured material properties of as-built and machined θ = 90° coupons

Coupon	t_{nom} (mm)	E (MPa)	$\sigma_{0.2}$ (MPa)	$\sigma_{1.0}$ (MPa)	σ_u (MPa)	ε_u	n	$m_{1.0}$	m_u
As-built	3.5	90200	261	319	448	0.119	6.5	2.5	2.6
	8.0	109100	271	326	423	0.103	5.5	2.6	2.5
Machined	3.5/8.0	139600	338	381	554	0.297	6.8	2.3	2.7

3. Manufacture of test specimens

The test specimens were wire arc additively manufactured by MX3D using their proprietary WAAM system, featuring a six-axis ABB robot and a metal inert gas (MIG) welder. 3D CAD models of the specimens were created and sliced into a series of layers to define the deposition paths. Following the planned build paths, the robot deposited successive layers of material to build up the tubular specimens. In this fashion, tubular sections of 3.5 mm and 8.0 mm nominal thickness t_{nom} were printed, using Grade 308LSi austenitic stainless steel feedstock wire with diameters of 1.0 mm and 1.2 mm, respectively. The chemical and mechanical properties of the feedstock material, as well as the WAAM process parameters, have been reported by Kyvelou et al. (2020).

After printing, each WAAM tube was detached from the substrate plate using a plasma arc cutter, and was cut using a rotary hacksaw to a length of about five times the maximum cross-sectional dimension, such that the obtained specimens were sufficiently long to include representative residual stress and local imperfection patterns and to allow the development of local buckling without any significant boundary effects (). The specimens, which included square, rectangular and irregular hollow sections, are shown after fabrication in Fig. 2. The specimen labelling system begins with the cross-section shape (‘S’, ‘R’ and ‘IR’ for square, rectangular and irregular hollow sections, respectively), followed by the nominal cross-sectional dimensions (height × breadth of compression flange × wall thickness) and member length in mm; the number at the end of a specimen label denotes the test ID, omitted if there was no repeat test.

Figure 2: WAAM specimens of square, rectangular and irregular hollow sections

4. Geometric measurements

The geometry and local imperfections of the WAAM specimens were examined before testing. 3D laser scanning, in conjunction with silicone casting, was used to capture both the external and internal surface profiles of the tubular specimens, with the scan data verified against volume measurements based on Archimedes' principle. In parallel with geometric characterization, the local imperfections of the specimens were also determined from the 3D scan data, as described in this section.

4.1 Geometric properties

Archimedes' measurements were taken to determine the volume of the specimens. Upon determination of the volume of each specimen, the average cross-sectional area A_{Arch} was derived by dividing the volume by the member length L, measured using calipers. In order to comprehensively capture the geometric details of the WAAM specimens, 3D laser scanning was employed, as shown in Fig. 3. The outer surface of each specimen was fully scanned, while direct scanning of the complete inner surface was precluded by the size of scanning arm head. A scannable replica of the interior geometry was therefore produced by means of silicone casting. The silicone casts were made of SUPERSIL 25, a two-component (base and catalyst) silicone elastomer, and were produced following the procedure illustrated in Fig. 4.

Figure 3: Laser scanning of a typical specimen

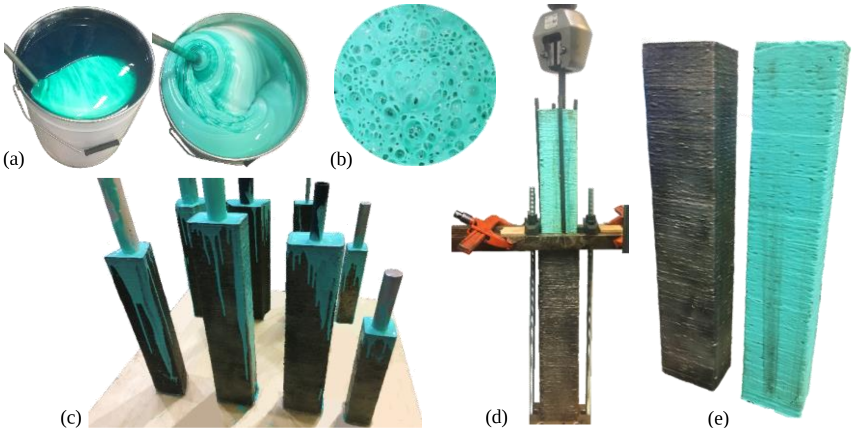

Figure 4: Production procedure of silicone casts: (a) preparing silicone mixture; (b) degassing; (c) casting silicone and curing; (d) extracting a silicone cast; (e) a silicone cast and its parent specimen

Upon extraction from within their parent specimens, the silicone casts were laser scanned; the resulting scans were merged with the outer scans of the tubes using Geomagic Wrap to create complete 3D scan models of the test specimens. The models were then converted into polygon objects and imported into Rhino 3D for further geometric analysis. A summary of the cross-sectional dimensions derived from the laser scans, along with the member length L, is presented in Table 2, where A, A_{max}, A_{min} are the average, maximum and minimum cross-sectional areas respectively, t and t_{sd} are the mean and standard deviation of the thickness respectively, and H, B, R, r are the height, breadth, outer corner radius and inner corner radius of the square and rectangular hollow sections (SHS and RHS) respectively. For the four irregular hollow sections, the outer cross-sectional dimensions are given in Fig. 5.

Table 2: Average measured geometric properties of WAAM tubular beams

Specimen	H (mm)	B (mm)	R (mm)	r (mm)	t (mm)	t_{sd} (mm)	A (mm^2)	A_{Arch} (mm^2)	L (mm)	w_0 (mm)
S150×150×3.5-750	149.7	149.4	8.6	4.7	4.13	0.53	2360.0	2385.6	749.8	2.39
S120×120×3.5-600	119.9	119.7	8.5	4.4	4.00	0.50	1795.0	1846.3	600.3	1.13
S110×110×3.5-550	110.0	109.8	8.5	4.3	3.84	0.46	1638.2	1616.9	549.7	0.73
S105×105×3.5-525	104.8	104.8	8.3	4.2	4.00	0.49	1554.3	1600.3	525.3	1.22
S100×100×3.5-500-1	99.8	99.6	8.1	4.3	4.01	0.44	1493.1	1527.5	500.0	0.58
S100×100×3.5-500-2	99.6	99.8	8.5	4.8	3.95	0.47	1476.0	1493.1	500.1	1.95
S70×70×3.5-340-1	70.2	70.0	8.3	4.4	4.00	0.54	1032.4	1047.7	340.2	0.60
S70×70×3.5-340-2	70.0	70.0	8.3	4.4	3.98	0.49	1008.8	1037.8	340.0	0.97
R80×120×3.5-590	80.2	120.7	9.2	5.4	4.05	0.46	1501.7	1535.2	590.4	1.07
R75×110×8.0-550	75.9	115.8	9.1	5.2	6.12	0.53	2113.6	2131.4	550.3	0.84
IR55×95×3.5-500	See Fig. 5 for cross-sectional shapes and dimensions				3.66	0.68	1245.0	1245.7	500.0	1.55
IR130×100×3.5-500					3.60	0.66	1577.0	1578.6	500.2	1.59
IR45×75×3.5-500					3.71	0.67	906.0	923.3	499.6	1.43
IR90×100×3.5-500					3.80	0.63	1695.0	1670.3	500.0	1.34

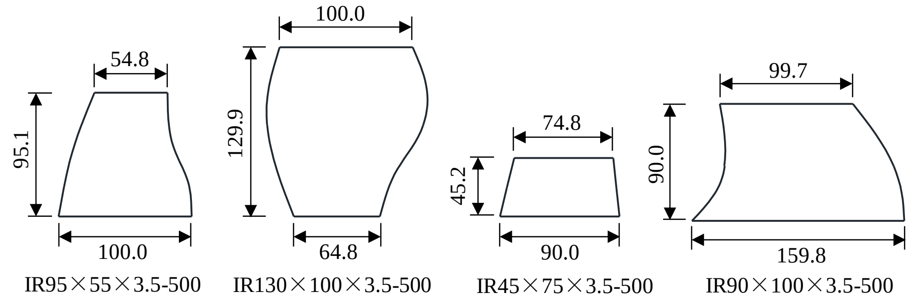

Figure 5: Measured outer cross-sectional dimensions (in mm) of irregular hollow section specimens

4.2 Local geometric imperfections

The local geometric imperfections of the WAAM specimens are examined in this section. As illustrated in Fig. 6, the local imperfections were determined using the grid points along the centerline of the specimen outer faces, in line with the approach proposed by Kyvelou et al. (2021). For each face, the local imperfection was defined as the deviation of each grid point from a straight line fitted to all the points along the member length using least squares regression, and the maximum deviation was taken as the local imperfection amplitude. This definition is deemed appropriate because the derived deviation corresponds to the out-of-flatness along the longitudinal axis of the structural elements; this out-of-flatness triggers and amplifies local plate buckling and thus governs the ultimate cross-section strength. However, the presence of some particularly prominent surface undulations and weld beads introduced by WAAM could lead to unrealistically large imperfection amplitude measurements. To filter these unwanted features, while retaining the underlying imperfection profiles, a 10 mm moving average was applied to smooth the obtained imperfection distributions. The maximum deviation of each smoothed curve from the fitted reference line was then taken as the local imperfection amplitude for the corresponding face. The obtained local imperfection amplitude of the compression flange of each beam specimen w_0 is reported in Table 2.

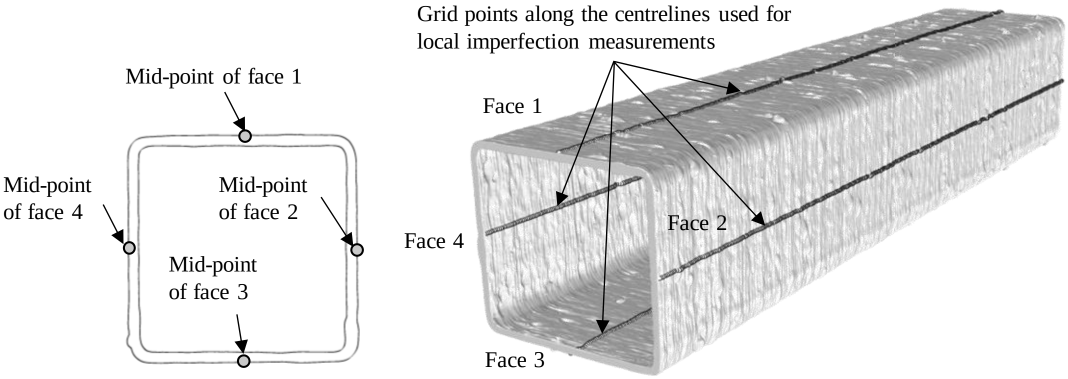

Figure 6: Determination of local geometric imperfections

5. Four-point bending tests

A total of 14 WAAM beam specimens, comprising eight SHS, two RHS and four irregular hollow sections, with a wide range of local slendernesses, were tested to investigate their cross-sectional behavior under uniform bending.

5.1 Test set-up

Prior to testing, each WAAM specimen was welded to two steel end plates and then bolted to a high-strength steel SHS at each end to extend the member length. All extended specimens were tested in the four-point bending configuration shown in Fig. 7, with the central WAAM tube located within the constant moment region. The specimens were simply supported on a pair of steel rollers, and symmetrically loaded through two further steel rollers. The vertical load was applied using an Instron 2000 kN hydraulic actuator, and transferred to the specimens through a special bearing, a spreader beam and the top two rollers. Rubber sheets were used to spread the loads onto the high-strength steel SHS, inside which wooden blocks were also inserted to prevent web crippling at the loading points and supports. A range of instrumentation was employed during the tests, including four load cells (two for each roller) to measure the applied vertical loads, four inclinometers to measure the rotations at the loading points and supports, and three string potentiometers to measure the vertical displacements at the mid-span and both ends of the WAAM specimens.

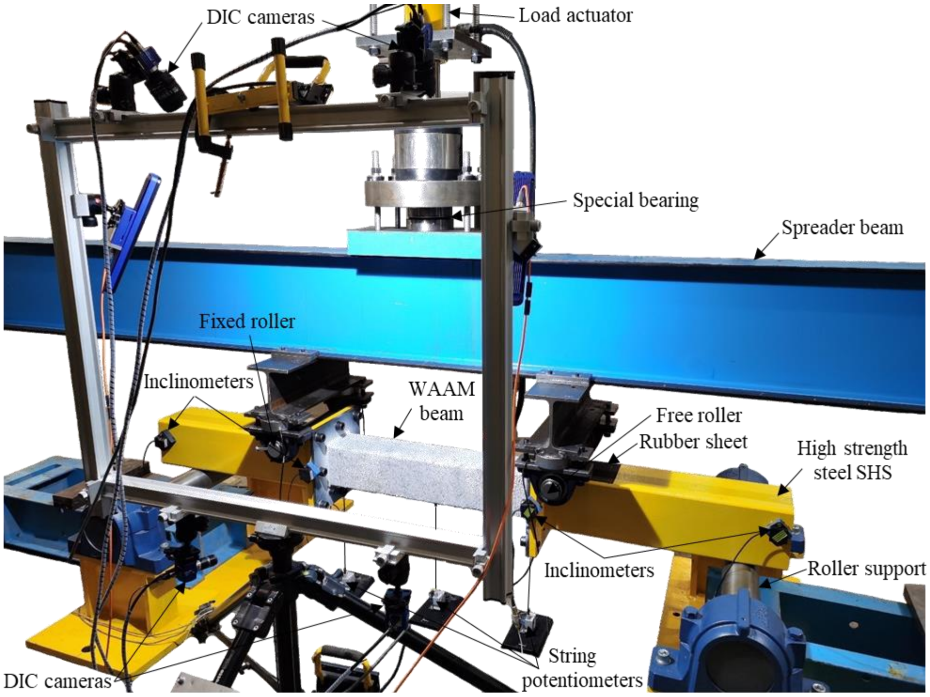

Figure 7: Determination of local geometric imperfections

5.2 Test results

The key results from the four-point bending tests are summarized in Table 3, including the measured ultimate bending moment Mu, the elastic and plastic moment capacities M_{el} and M_{pl}, taken as the product of the 0.2% proof stress $\sigma_{0.2}$ and the elastic and plastic section modulus respectively, the normalized ultimate moment ($M_{\mathrm{u}}/M_{\mathrm{el}}$ and $M_{\mathrm{u}}/M_{\mathrm{pl}}$), the curvature at the ultimate moment κ_{u}, the elastic curvature at the plastic moment κ_{pl}, the curvature when the applied moment falls back to the plastic moment $\kappa_{\mathrm{pl,u}}$, and the cross-sectional rotation capacity R. The local slenderness of the compression flange, which is the dominant element in determining the local stability of the studied cross-sections, $c/t\varepsilon$, where c is the compressed flat width, t is the plate thickness and $\varepsilon = \sqrt{(235/\sigma_{0.2})/(E/210000)}$, is also reported in Table 3 for all beam specimens. Note that M_{el}, M_{pl} and ε were calculated based on the mechanical properties of the as-built material, as given in Table 1. The normalised moment–curvature curves M/M_{pl}–κ/κ_{pl} for all tests are shown in Fig. 8. All tested WAAM beams displayed local buckling of the compression flange and the upper portion of the webs. The location of failure (i.e. local buckling) in the specimens related to the geometric imperfection distributions and thickness variations. This can be seen in Fig. 9, where the distributions of the local geometric imperfections w and average wall thickness of the compression flange t_c along the member length for two typical specimens (covering two nominal thicknesses) are shown, along with the longitudinal strain distribution over the side face of each specimen from the DIC results to highlight the failure location.

Table 3: Summary of key results for WAAM tubular beams

Specimen	$c/t\varepsilon$	M_u (kNm)	M_{el} (kNm)	M_{pl} (kNm)	κ_u (×10^{-4} mm^{-1})	κ_{pl} (×10^{-4} mm^{-1})	$\kappa_{pl,u}$ (×10^{-4} mm^{-1})	M_u/M_{el}	M_u/M_{pl}	R
S150×150×3.5-750[1]	51.5	28.0	28.7	33.4	0.84	0.45	–	0.97	0.84	0.00
S120×120×3.5-600	41.3	21.1	17.4	20.3	1.61	0.56	2.01	1.21	1.04	2.56
S110×110×3.5-550	38.9	18.3	13.9	16.3	1.74	0.62	3.13	1.32	1.13	4.07
S105×105×3.5-525	35.4	15.6	13.0	15.3	1.92	0.65	2.25	1.20	1.02	2.47
S100×100×3.5-500-1	33.4	15.3	11.8	13.9	2.87	0.68	5.06	1.30	1.10	6.41
S100×100×3.5-500-2	33.7	14.0	11.6	13.6	1.94	0.68	3.24	1.21	1.03	3.73
S70×70×3.5-340-1[2]	21.5	8.4	5.4	6.5	17.87	0.99	21.07	1.56	1.30	>20.25
S70×70×3.5-340-2[2]	21.6	7.6	5.3	6.4	7.19	0.99	16.95	1.42	1.18	>16.07
R80×120×3.5-590	40.6	11.9	10.4	12.0	2.04	0.83	2.04	1.15	1.00	0.00
R75×110×8.0-550	23.8	16.9	13.7	16.3	4.43	0.61	6.88	1.23	1.04	10.36
IR55×95×3.5-500[2]	17.1	12.4	7.8	10.1	5.16	0.72	7.86	1.59	1.22	>9.97
IR130×100×3.5-500[1]	37.5	17.1	13.4	17.3	1.09	0.53	–	1.28	0.99	0.00
IR45×75×3.5-500	25.6	4.2	3.3	3.9	3.95	1.47	6.80	1.25	1.07	3.63
IR90×100×3.5-500	35.5	16.0	11.8	13.6	1.95	0.69	4.37	1.36	1.18	5.32

1. Test moment failed to reach M_{pl} ($M_u < M_{pl}$).
2. Test terminated before moment fell below M_{pl} on descending curve.

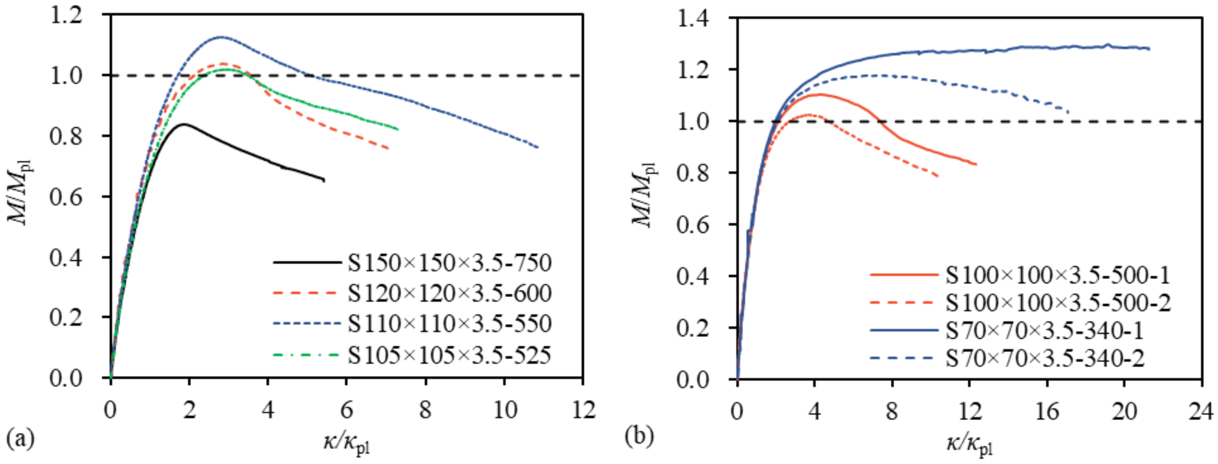

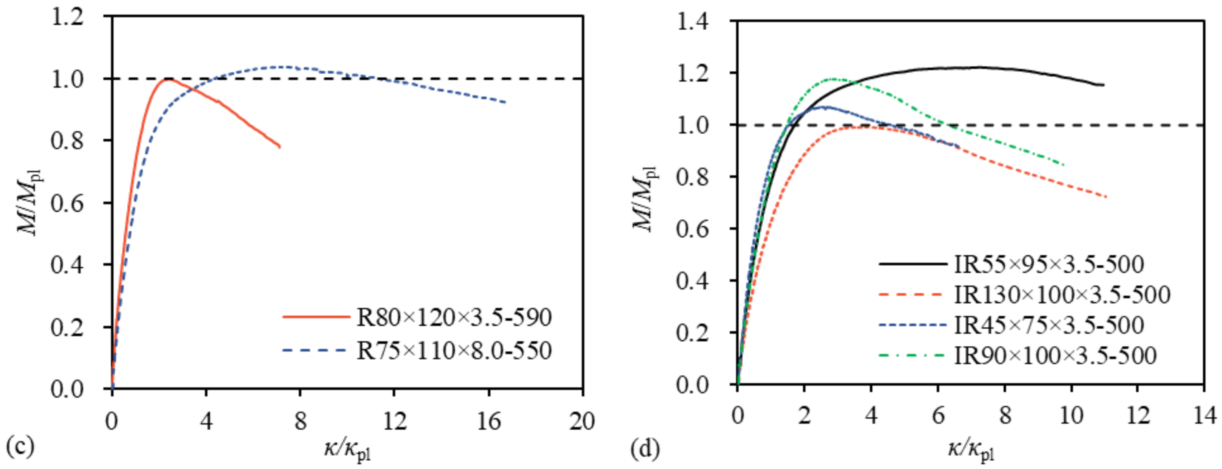

Figure 8: Normalized moment–curvature curves of tested beams: (a, b) SHS; (c) RHS; (d) irregular hollow sections.

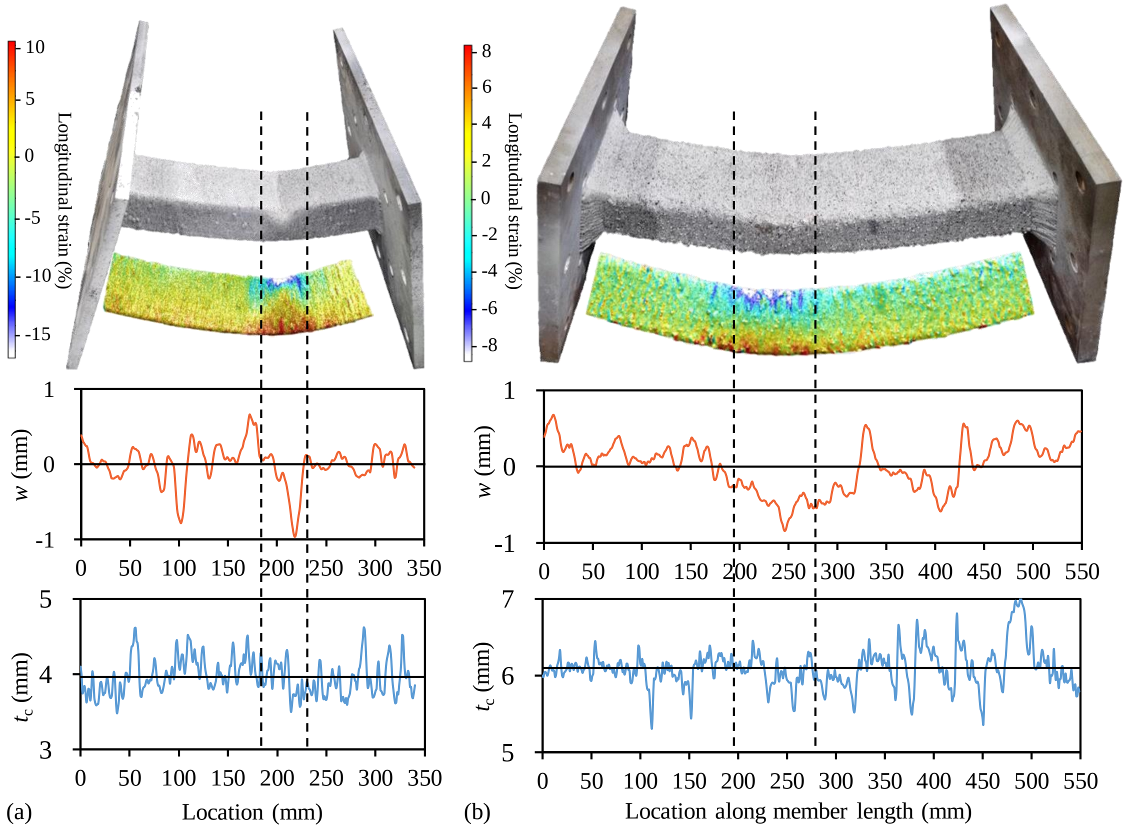

Figure 9: Typical failure models of test specimens and correlation between geometric variability and failure locations, shown for Specimens (a) S70×70×3.5-340-2 and (b) R75×110×8.0-550.

6. Comparisons with existing design methods

In this section, the test results are used to assess the applicability of existing cross-section design methods to WAAM stainless steel tubular beams. The suitability of the local slenderness limits specified in the current European and American standards is first assessed. The test results are subsequently compared against the cross-section resistance predictions from the design functions of EN 1993-1-4, AISC 370 and the continuous strength method (CSM) to assess their applicability to the design of WAAM sections in bending.

6.1 Assessment of local slenderness limits

Assessment of the Class 1 slenderness limit was carried out on the basis of a rotation capacity requirement of R = 3, which is widely adopted for the plastic design of steel structures. The rotation capacities R of the tested WAAM sections are plotted against the local slenderness parameter $c/t\varepsilon$ (calculated based on the as-built material properties) in Fig. 10, where test data on conventionally produced stainless steel sections collected from the literature (Theofanous et al. 2010; Afshan et al. 2013; Bock et al. 2015; Zhao et al. 2015) and the AISC compact slenderness limit are also depicted for comparison purposes. The collected rotation capacity data points are rather scattered, due mainly to the varying stainless steel grades, levels of geometric imperfections and moment gradients, as well as to the interaction of constituent plate elements. However, the WAAM beam data can be seen to follow a similar trend to the conventional beam data and the current EC3 Class 1 slenderness limit of $c/t\varepsilon$ = 33 is on the safe side.

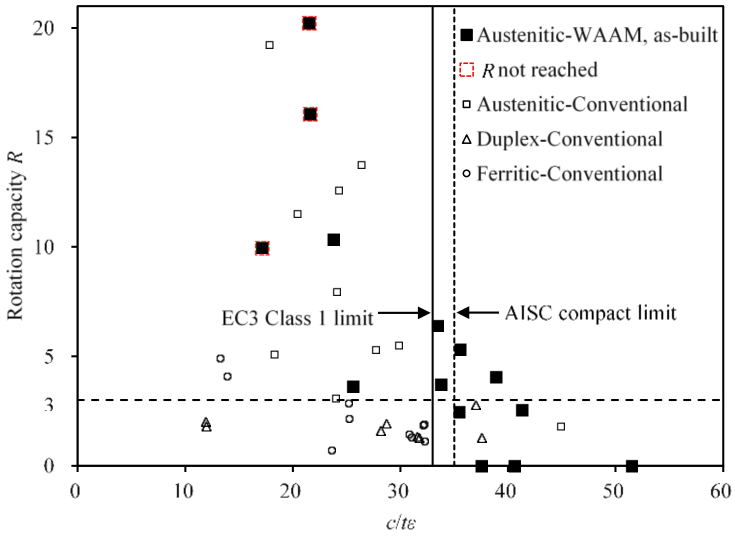

Figure 10: Assessment of EC3 Class 1 and AISC compact slenderness limits

The experimental ultimate moment capacities M_u obtained from this study are normalised by the plastic moment capacities M_{pl} and plotted against the $c/t\varepsilon$ ratio of the compression flange in Fig. 11, where the collected test data on conventionally manufactured stainless steel beams (Theofanous et al. 2010; Afshan et al. 2013; Bock et al. 2015; Zhao et al. 2015), as well as the EC3 Class 2 slenderness limit and AISC compact slenderness limit, are also depicted. Both the as-built and machined material properties, as given in Table 1, are used for the normalization and analysis of the test data on the WAAM sections. It is shown that the data points associated with the machined material properties consistently lie below the collated test dataset of conventionally produced sections. In contrast, use of the as-built material properties, which incorporate the effect of the geometric undulations, results in the WAAM data points generally lying within the range of the test data on the conventionally formed sections. With the adoption of the as-built material properties, the EC3 Class 2 and AISC compact slenderness limit of 35 appears to be suitable for WAAM plate elements in compression.

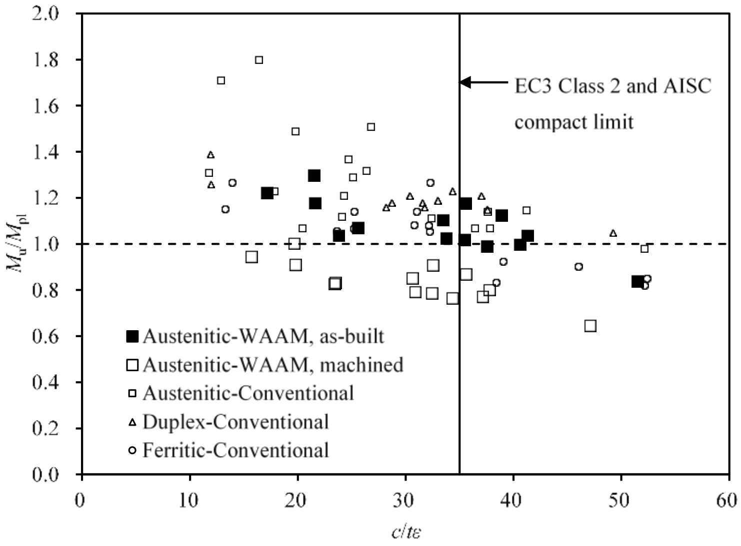

Figure 11: Assessment of EC3 Class 1 and AISC compact slenderness limits

To appraise the suitability of the EC3 Class 3 limit and AISC noncompact slenderness limit for internal compression elements, the bending test results from this study, together with the compression test results on WAAM sections from a previous study (Kyvelou et al. 2021) and the collected test data on conventionally produced stainless steel beams, are shown in Fig. 12, where the ultimate moment capacity normalized by the elastic moment capacity M_u/M_{el} (for beams) and the ultimate load capacity normalized by the yield load $N_u/A\sigma_{0.2}$ (for stub columns) are plotted against the local slenderness parameter $c/t\varepsilon$. From Fig. 12, it can be observed that the EC3 Class 3 and AISC noncompact slenderness limit of 37, and the CSM yield slenderness limit of 38.6, appear to be generally applicable to WAAM sections in compression and bending. Overall, Figs 10-12 demonstrate a clear trend between an increasing local slenderness and a decreasing rotation capacity and normalized moment capacity. The current codified slenderness limits are shown to be generally applicable to the examined WAAM tubular beams, provided that the influence of the surface undulations associated with as-built WAAM elements are accounted for through the use of material properties derived from coupons tested in the as-built condition.

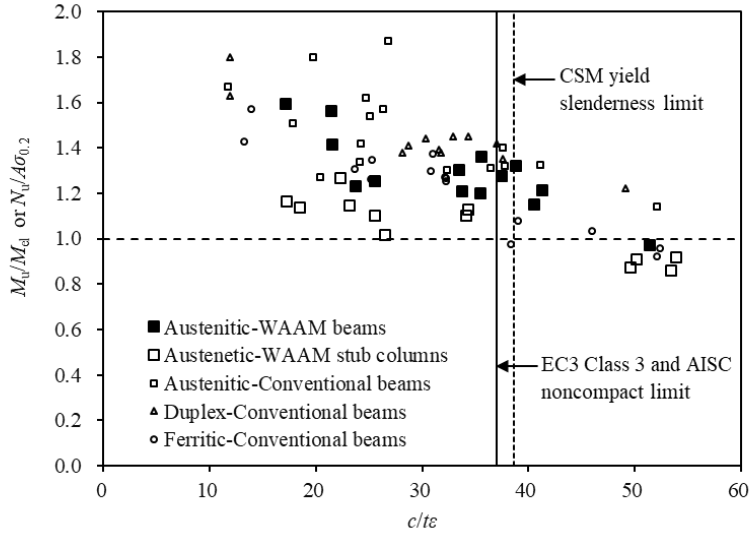

Figure 12: Assessment of EC3 Class 3, AISC noncompact and CSM yield slenderness limits

6.2 Assessment of resistance predictions

In this subsection, the cross-section resistances of the tested WAAM beams are compared against the cross-section resistances predicted using the EC3, AISC and CSM design functions. Based on the aforementioned cross-sectional classifications, the unfactored design resistances for bending about one principal axis of a cross-section (MEC3 and MAISC) are given by Eqs (1)-(3) in EN 1993-1-4:

$$M_{\mathrm{EC3}} = M_{\mathrm{pl}} = W_{\mathrm{pl}}\sigma_{0.2} \text{ for Class 1 and 2 cross-sections} \tag{1}$$

$$M_{\mathrm{EC3}} = M_{\mathrm{el}} = W_{\mathrm{el}}\sigma_{0.2} \text{ for Class 3 cross-sections} \tag{2}$$

$$M_{\mathrm{EC3}} = W_{\mathrm{eff}}\sigma_{0.2} \text{ for Class 4 cross-sections} \tag{3}$$

where W_{el}, W_{pl} and W_{eff} are the elastic, plastic and effective section moduli, respectively, and Eqs (4)-(6) in AISC 370, where the notation has been harmonized between the specifications for simplicity.

$$M_{\mathrm{AISC}} = M_{\mathrm{pl}} = W_{\mathrm{pl}}\sigma_{0.2} \text{ for compact cross-sections} \tag{4}$$

$$M_{\mathrm{AISC}} = M_{\mathrm{pl}} - (M_{\mathrm{pl}} - M_{\mathrm{el}})\left(\frac{\lambda - \lambda_{\mathrm{pf}}}{\lambda_{\mathrm{rf}} - \lambda_{\mathrm{pf}}}\right) \text{ for noncompact cross-sections} \tag{5}$$

$$M_{\mathrm{AISC}} = W_{\mathrm{eff}}\sigma_{0.2} \text{ for slender cross-sections} \tag{6}$$

where $\lambda = c/t\varepsilon$ is the local slenderness, and λ_{pl} and λ_{rl} are the slenderness limits for compact and noncompact flanges, equal to 35 and 37, respectively.

The continuous strength method (CSM) is a deformation-based design approach featuring two key components: (1) a base curve to provide a non-dimensional measure of cross-section deformation (strain) capacity and (2) a material model, which allows for strain hardening and, in conjunction with the strain measure, can be used to determine the cross-section bending resistance. The base curve adopted herein for SHS/RHS is given by Eq. (7), comprising two parts: for non-slender ($\bar{\lambda}_{\mathrm{p,c}} \leq 0.68$) and slender ($0.68 < \bar{\lambda}_{\mathrm{p,c}} \leq 1.6$) cross-sections respectively:

$$\frac{\varepsilon_{\mathrm{csm}}}{\varepsilon_{\mathrm{y}}} = \begin{cases} \dfrac{0.25}{\bar{\lambda}_{\mathrm{p,cs}}^{3.6}} \leq \min\left(15, \dfrac{0.1\varepsilon_{\mathrm{u}}}{\varepsilon_{\mathrm{y}}}\right) & \text{for } \bar{\lambda}_{\mathrm{p,cs}} \leq 0.68 \\ \left(1 - \dfrac{0.222}{\bar{\lambda}_{\mathrm{p,cs}}^{1.05}}\right)\dfrac{1}{\bar{\lambda}_{\mathrm{p,cs}}^{1.05}} & \text{for } 0.68 < \bar{\lambda}_{\mathrm{p,cs}} \leq 1.6 \end{cases} \tag{7}$$

where $\varepsilon_{\mathrm{csm}}$ is the limiting strain (i.e. the deformation capacity) of the cross-section, ε_{y} and ε_{u} are the material yield and ultimate strains, respectively, and $\bar{\lambda}_{\mathrm{p,c}}$ is the slenderness of the full cross-section, defined by:

$$\bar{\lambda}_{\mathrm{p,cs}} = \sqrt{\frac{M_{\mathrm{el}}}{M_{\mathrm{cr}}}} \tag{8}$$

where M_{cr} is the elastic local buckling moment, obtained using numerical software ABAQUS. The material model for austenitic stainless steel sections is given by Eqs (9) and (10):

$$E_{\mathrm{sh}} = (\sigma_{\mathrm{u}} - \sigma_{0.2}) / (0.16\varepsilon_{\mathrm{u}} - \varepsilon_{\mathrm{y}}) \tag{9}$$

$$\varepsilon_{\mathrm{u}} = (1 - \sigma_{0.2} / \sigma_{\mathrm{u}}) \tag{10}$$

where E_{sh} is the strain hardening modulus. Combining the CSM base curve and material model, the cross-section moment resistance M_{csm} is determined from Eq. (11):

$$M_{\mathrm{csm}} = \begin{cases} W_{\mathrm{pl}}\sigma_{0.2}\left[1 + \dfrac{E_{\mathrm{sh}}}{E}\dfrac{W_{\mathrm{el}}}{W_{\mathrm{pl}}}\left(\dfrac{\varepsilon_{\mathrm{csm}}}{\varepsilon_{\mathrm{y}}} - 1\right) - \left(1 - \dfrac{W_{\mathrm{el}}}{W_{\mathrm{pl}}}\right) / \left(\dfrac{\varepsilon_{\mathrm{csm}}}{\varepsilon_{\mathrm{y}}}\right)^{2}\right] & \text{for } \bar{\lambda}_{\mathrm{p,cs}} \le 0.68 \\ \dfrac{\varepsilon_{\mathrm{csm}}}{\varepsilon_{\mathrm{y}}} W_{\mathrm{el}}\sigma_{0.2} & \text{for } 0.68 < \bar{\lambda}_{\mathrm{p,cs}} \le 1.6 \end{cases} \tag{11}$$

The test ultimate moment capacities M_{u} are compared with the EN 1993-1-4, AISC 370 and CSM resistance predictions $M_{\mathrm{u,pred}}$ calculated based on the as-built material properties; the comparisons are plotted in Fig. 13 and reported in Table 4. The graphical and numerical comparisons show that the EC3, AISC and CSM design approaches generally yield safe-sided strength predictions for the WAAM beams. Based on the concept of placing cross-sections into behavioral classes, the current design provisions of EN 1993-1-4 and AISC 370 yield comparable moment resistance predictions; the only major difference lies in the design of Class 3 (AISC noncompact) cross-sections, where the AISC design method offers improved design accuracy and efficiency over the elastic EC3 method by means of utilization of partial plasticization in bending. The CSM allows for a rational exploitation of the spread of plasticity and material strain hardening, and thus, as expected, provides more accurate and consistent strength predictions than those from the EC3 and AISC design approaches.

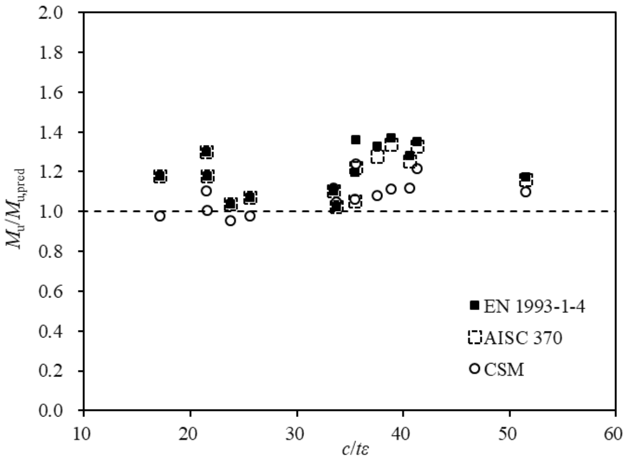

Figure 13: Comparison of test results with EN 1993-1-4, AISC 370 and CSM strength predictions

Table 4: Comparisons of test results with predicted moment resistances for tubular beams.

Specimen	EC3 Class	AISC Class	$c/t\varepsilon$	$\bar{\lambda}_{p,EC3}$	$\bar{\lambda}_{p,AISC}$	$\bar{\lambda}_{p,cs}$	M_u/M_{EC3}	M_u/M_{AISC}	M_u/M_{csm}
S150×150×3.5-750	4	Slender	51.5	0.94	0.91	0.84	1.17	1.16	1.10
S120×120×3.5-600	4	Slender	41.3	0.76	0.73	0.68	1.35	1.33	1.22
S110×110×3.5-550	4	Slender	38.9	0.72	0.68	0.65	1.37	1.34	1.12
S105×105×3.5-525	3	Noncompact	35.4	0.66	0.62	0.59	1.20	1.05	1.06
S100×100×3.5-500-1	2	Compact	33.4	0.62	0.59	0.56	1.10	1.10	1.12
S100×100×3.5-500-2	2	Compact	33.7	0.63	0.59	0.57	1.03	1.03	1.05
S70×70×3.5-340-1	1	Compact	21.5	0.41	0.38	0.39	1.30	1.30	1.11
S70×70×3.5-340-2	1	Compact	21.6	0.41	0.38	0.39	1.18	1.18	1.01
R80×120×3.5-590	4	Slender	40.6	0.76	0.71	0.66	1.28	1.25	1.12
R75×110×8.0-550	1	Compact	23.8	0.45	0.42	0.43	1.04	1.04	0.95
IR55×95×3.5-500	1	Compact	17.1	0.34	0.30	0.35	1.18	1.18	0.98
IR130×100×3.5-500	4	Slender	37.5	0.70	0.66	0.60	1.33	1.28	1.08
IR45×75×3.5-500	1	Compact	25.6	0.49	0.45	0.44	1.07	1.07	0.98
IR90×100×3.5-500	3	Noncompact	35.5	0.66	0.63	0.61	1.36	1.22	1.24
Mean							1.21	1.18	1.08
COV							0.10	0.09	0.08

7. Conclusions

An experimental program has been undertaken to investigate the cross-sectional behavior of WAAM stainless steel tubular beams. Four-point bending tests on a total of 14 square, rectangular and irregular tubular cross-sections, covering a wide range of local slenderness values, have been conducted. Similar to equivalent, conventionally formed sections, the tested WAAM beams revealed the anticipated trend of decreasing normalized moment capacity and rotation capacity with increasing local slenderness, reflecting increasing susceptibility to local buckling. However, owing to the inherently greater variation in geometry, the WAAM beams exhibited more variable flexural capacities between repeat specimens than generally displayed by conventionally produced stainless steel sections. The test results were used to assess the applicability of the cross-section design provisions in EN 1993-1-4 and AISC 370 as well as the continuous strength method (CSM) to WAAM stainless steel tubular beams. On the basis of the as-built material properties, the current codified local slenderness limits were shown to be generally applicable to WAAM sections in bending; the EC3, AISC and CSM design approaches generally yielded safe-sided strength predictions for WAAM tubular beams, with the CSM providing the most accurate and consistent results. Further test data are nonetheless considered necessary to confirm the findings and assess the reliability. The presented results lay the foundations for the development of numerical models alongside more suitable structural design rules for WAAM elements in future research.

Acknowledgments

This research was possible thanks to the Engineering and Physical Sciences Research Council (EPSRC) funding under Grant No. EP/R010161/1 and from the UK Collaboratorium for

Research on Infrastructure and Cities (UKCRIC) Coordination Node EPSRC grant under EP/R017727/1.

References

Afshan S., Gardner L. (2013). "Experimental study of cold-formed ferritic stainless steel hollow sections." *Journal of Structural Engineering*, 139:717-28.

ASTM International. (2017). "Additive manufacturing—general principles—terminology." ISO/ASTM 52900, West Conshohocken, PA.

AISC 370. (2020). "Specification for structural stainless steel buildings." American Institute of Steel Construction (AISC), Chicago, Illinois.

Bock M., Arrayago I., Real E. (2015). "Experiments on cold-formed ferritic stainless steel slender sections." *Journal of Constructional Steel Research*, 109:13-23.

EN 1993-1-4:2006+A1:2020. (2020). "Eurocode 3—Design of Steel Structures—Part 1-4: General Rules—Supplementary Rules for Stainless Steel." CEN (European Committee for Standardization), Brussels.

Gardner, L. (2023). "Metal additive manufacturing in structural engineering–review, advances, opportunities and outlook." *Structures*,47: 2178-2193.

Gardner L., Kyvelou P., Herbert G., Buchanan C. (2020). "Testing and initial verification of the world's first metal 3D printed bridge." *Journal of Constructional Steel Research*,172:106233.

Huang C. (2022a). "Material and structural behaviour of metal 3D printed elements." Imperial College London, (PhD thesis).

Huang C., Kyvelou P., Zhang R., Britton T.B., Gardner L. (2022b). "Mechanical testing and microstructural analysis of wire arc additively manufactured steels." *Materials & Design*, 216:110544.

Huang C., Meng X., Gardner L. (2022c). "Cross-sectional behaviour of wire arc additively manufactured tubular beams." *Engineering Structures*, 272:114922.

Huang C., Meng X., Buchanan C., Gardner L. (2022d). "Flexural buckling of wire arc additively manufactured tubular columns." *Journal of Structural Engineering*, 148:04022139.

Huang C., Kyvelou P., Gardner L. (2023). "Stress-strain curves for wire arc additively manufactured steels." *Engineering Structures*, (In press). https://doi.org/10.1016/j.engstruct.2023.115628.

Kyvelou P., Slack H., Mountanou D.D., Wadee M.A., Britton T.B., Buchanan C., Gardner L. (2020). "Mechanical and microstructural testing of wire and arc additively manufactured sheet material." *Materials & Design*,192:108675.

Kyvelou P., Huang C., Gardner L., Buchanan C. (2021). "Structural testing and design of wire arc additively manufactured square hollow sections." *Journal of Structural Engineering*, 147:1-19.

Mirambell E., Real E. (2000). "On the calculation of deflections in structural stainless steel beams: an experimental and numerical investigation." *Journal of Constructional Steel Research*, 54:109-33.

Ramberg W., Osgood W. R. (1943). "Description of stress-strain curves by three parameters." Technical Note No. 902, National Advisory Committee for Aeronautics. Washington, D.C., USA.

Theofanous M., Gardner L. (2010). "Experimental and numerical studies of lean duplex stainless steel beams." *Journal of Constructional Steel Research*, 66:816-25.

Zhao O., Rossi B., Gardner L., Young B. (2015). "Behaviour of structural stainless steel cross-sections under combined loading - Part I: Experimental study." *Engineering Structures*, 89:236-46.

Ziemian R.D. (2010). "Guide to stability design criteria for metal structures." 6th ed. Hoboken, New Jersey: John Wiley & Sons, Inc.